Performance Projections for Ballistic Graphene Nanoribbon Field-Effect Transistors

Gengchiau Liang *Member, IEEE*, Neophytos Neophytou *Student Member, IEEE*, Dmitri E. Nikonov *Senior Member, IEEE*, and Mark S. Lundstrom *Fellow, IEEE*

This work was supported by the MARCO Focus Center on Materials, Structures, and Devices and the Semiconductor Research Corporation.
G. Liang, N. Neophytou, and M. S. Lundstrom are with the School of Electrical and Computer Engineering, Purdue University, West Lafayette, Indiana 47907-1285. (Phone: 765-494-9034; Fax: 765-404-6441; e-mail: liangg@purdue.edu)
D. E. Nikonov is with the Technology and Manufacturing Group, Intel Corp., SC1-05, Santa Clara, California 95052.

Abstract

The upper limit performance potential of ballistic carbon nanoribbon MOSFETs is examined. We calculate the bandstructure of nanoribbons using a single p_z-orbital tight-binding method and evaluate the current-voltage characteristics of a nano-ribbon MOSFET using a semiclassical, ballistic model. We find that semiconducting ribbons a few nanometers in width behave electronically in a manner similar to carbon nanotubes, achieving similar ON-current performance. Our calculations show that semiconducting carbon nanoribbon transistors can be candidates for high mobility digital switches, with the potential to outperform the silicon MOSFET. Although wide ribbons have small bandgaps, which would increase subthreshold leakage due to band to band tunneling, their ON-current capabilities could still be attractive for certain applications.

Index Terms—MOSFET, quantum confinement, carbon, graphite, nanotechnology, current density, nanowire, bandstructure, ballistic

I. INTRODUCTION

Carbon nanotubes (CNTs) have recently attracted broad attention for future electron device applications because of their excellent electronic [1] and optical [2] characteristics. Prototype structures showing good performance for transistors [3], interconnects [4], electromechanical switches [5], infrared emitters [2], and bio-sensors [6] have been demonstrated. To use CNT metal-oxide-semiconductor field-effect-transistors (MOSFETs) in realistic IC applications, however, material properties such as the bandgap (E_G) have to be precisely controlled. Although the presence of absence of a bandgap is a strong function of its chirality [7], there is currently no straightforward way to control the CNT chirality during growth.

The carbon nanoribbon metal-oxide-semiconductor field-effect-transistor (CNR MOSFET) is an alternative device possibility that could bypass the CNT chirality challenge. Carbon nanoribbons (CNRs) are graphene sheet monolayers patterned along a specific channel transport direction with a narrow channel width. They are theoretically expected to exhibit promising electronic properties [8] and extremely high electron/hole mobility [9], similar to the properties observed in CNTs. A CNR MOSFET is a device that would utilize a CNR as the channel of a FET-like device. Graphene is, of course, known to be a semi-metal, but the spatial confinement of the ribbons in their transverse direction can induce a bandgap. The width of the ribbon (in the transverse direction) and its transport orientation relative to the graphene crystal structure are the two parameters that determine the bandgap and the electronic properties of the CNR [10], in a similar way that the chirality controls the properties of the CNT. In the case of the CNR MOSFETs, however, the possibility to pattern the nanoscale strip of graphene which has

a definite orientation relative to the substrate [11] is a possible way to overcome the CNT chirality control problem. The ultra-thin carbon monolayer, furthermore, would provide extremely good gate electrostatic control. In this sense, the CNR MOSFET would be the ultimate two-dimensional (2D) device, and is expected to greatly reduce short channel effects such as drain induced barrier lowering (DIBL) and subthreshold swing (S), which are mainly determined by the electrostatics of the device. The control over these parameters plays an important role in nanoscale MOSFET performance.

In this work, we analyze the electronic structure of CNRs with two different transport orientations, the armchair and zig-zag orientations as shown in Fig. 1. Note that the names "armchair" and "zig-zag" refer to the shape of the edge in the transport direction of the CNR and follow the standard CNR literature convention [8] which is opposite to the CNT convention [7]. We find that certain armchair CNRs can exhibit semiconducting behavior. Zig-zag CNRs are either metallic or semiconducting but with localized states appearing in the bandgap. In this study, we focus only on the armchair semiconducting CNRs since they appear to be the most promising for use as the channel of conventional MOSFETs. We then explore the ballistic current-voltage characteristics of semiconducting CNR MOSFETs. We find that narrow CNR devices can operate as digital switches and potentially outperform an ideal, ballistic Si MOSFET in terms of drive current capabilities.

II. APPROACH

In order to explore the performance potential of armchair CNR MOSFETs, we follow a two-step procedure. First, we assume a CNR with a certain width and orientation, and then we calculate its *E-k* relation. Next, we use the calculated dispersion relations to calculate the ballistic current-voltage (*I-V*) characteristics of n-channel CNR MOSFETs using a semi-classical "top-of-the-barrier" MOSFET model [12].

A. Electronic Bandstructure Calculations:

To calculate the dispersion relation of CNRs, we employ a nearest-neighbor orthogonal tight-binding (TB) method based on a single p_z-orbital. The Hamiltonian of the CNR (either armchair, or zig-zag) is given by:

$$H = \sum_{i,j} t_{i,j} \mid i >< j \mid , \tag{1}$$

where $t_{i,j}$ is the hopping parameter and $\mid i >$ ($\mid j >$) is a localized orbital on site *i(j)*. Throughout this work, $t_{i,j}$ is set to 3 eV [7] when *i* and *j* are nearest neighbors; and zero elsewhere. Due to the abrupt termination of the graphene layer, dangling bonds appear at the edge of the CNR that are assumed to be terminated by hydrogen atoms as shown in Fig. 1(a) and Fig. 1(d), respectively. The C-H bond state (σ state) will not impact the CNRs' electronic structure near the Fermi level because there is no interaction between the σ bond and π bond contributed by the p_z orbital. Therefore, the simple p_z-orbital model is still a valid method. More sophisticated approaches, such as extended Huckel theory (EHT) and first principle calculations [13], have demonstrated that near the Fermi level the bandstructure of CNRs with hydrogen atom termination is essentially identical to the results as TB p_z-orbital model calculations.

Next, based on the transport direction and the width of the CNR, the unit cell can be defined, cf. the dashed rectangle in Fig. 1(a) and (d). The Hamiltonian of the unit cell and its coupling with neighbors can be obtained from (1). We define this as H_l, where l is the unit cell index, which takes values $l = \pm 1$ for nearest-neighbor unit cells, and *0* for the center unit cell. The Hamiltonian in *1D* *k*-space corresponding to the direction along the CNR is the Fourier transform of H_l as follows:

$$H_{k_m} = \sum_l H_l \exp[-i \bullet k_m (z_l - z_0)], \tag{2}$$

where $k_m = m\pi/L$ is the wavevector, (where $m \in [0,1]$ and L is the length of the unit cell), and z_l is the unit cell position—i.e. $l \cdot L$. The dispersion relation is obtained by solving for eigenvalues of (2) for all *k*-points in the first Brillouin zone.

Both armchair and zigzag CNRs can have metallic or semiconducting electronic properties. For example, Fig. 1(b) shows the energy dispersion (*E*-*k*) relations of an armchair CNR with $N=9$ (N being the number of atoms in transverse direction) which exhibits semiconducting characteristics, while Fig. 1(c) shows a semi-metallic electronic structure of a same type of ribbon with $N=8$. Note that the degeneracy of the lowest subband is 1, unlike carbon nanotubes where the degeneracy is 2. This is caused by the “hard-wall” boundary conditions in nanoribbons rather than periodic boundary conditions see e.g. [9]. The semi-metallic armchair ribbon occurs when $N=3m-1$, where m is an integer [8]. Similarly, for armchair CNRs, Fig. 1(e) shows the metallic electronic structure of the zigzag CNR with $N=10$, whereas Fig. 1(f) shows the semiconductor bandstructure of a zigzag CNR with $N=9$. In the latter case, however, localized edge states appear in the bandgap. This kind of CNR appears when $N = 2m \pm 1$, where m is an integer, and has been referred as *“bearded ribbon”* [14]. These results are in very good

agreement with previous studies of CNR electronic structure [8-11]. In this work, we mainly focus on semiconducting armchair CNRs *(N=3m or 3m+1)* since they appear to be the most promising type to be used as a MOSFET.

B. Transport Calculation:

To explore the *I-V* characteristics of ballistic CNR MOSFETs, we employ a "top-of-the-barrier" MOSFET model [12]. This is a simple model which can, however, capture two-dimensional self-consistent electrostatics and quantum capacitance effects in ballistic MOSFETs. Band-to-band tunneling (responsible for ambipolar conduction) and source-to-drain tunneling (which is likely to be important for smaller bandgaps) are not accounted for in this model. As illustrated in Fig. 2(a), the charge at the top of barrier is computed directly from the *E-k* relations, i.e. (2), by filling the positive velocity states according to the source Fermi level and the negative velocity states according to the drain Fermi level by,

$$N = \int_0^{\infty} \frac{dk}{\pi}[f(E - E_{fs}) + f(E - E_{fs} + qV_D)], \tag{3}$$

where *f(E)* is the Fermi function and E_{fs} is the chemical potential in the source region. The carrier density calculation is self-consistently coupled to Poisson's equation solved at the top of the barrier through a simple capacitive model involving the gate insulator capacitance (C_G), the drain capacitance (C_D), and the source capacitance (C_S). In this work, we assume that, $C_G \gg C_D, C_S$, which means that the gate has perfect gate control over the channel. In this way, we minimize the amount of DIBL and obtain subthreshold swings close to the ideal 60mV/dec. Finally, the ballistic current is evaluated from the

difference between the positive and negative going fluxes after electrostatic/transport convergence is achieved. Details of the model are described in Ref. [12]. We concentrate on the ON-state ballistic performance of the device since subthreshold leakage due to band-to-band tunneling is not captured by this simple model.

In this paper, we assume our device structure to be a planar, top-gated N-channel CNR MOSFET with insulator thickness t_{ins}= 1.1 nm and dielectric constant κ=4, which results in a gate insulator capacitance of C_G = 31.4 fF/μm^2. The cross-section and top view of this hypothetical device are illustrated schematically in Fig. 2(b) and Fig. 2(c). The source and drain region are assumed to be heavily n-type doped nanoribbon extensions that are capable of supplying any current that the gate and drain voltages demand.

Since the bandgap and electronic properties of CNRs will depend on the size quantization in the transverse direction, we compare ideal, ballistic CNR MOSFETs with widths W=2.2 nm ($N=18$) and 4.2 nm ($N=35$) to an ideal, ballistic Si MOSFET whose device structure is specified by the 90 nm node of 2005 ITRS report [15]. We found that ideal ballistic CNR MOSFETs can outperform an ideal, ballistic MOSFET by up to 200% in terms of ON-current density at a fixed off current.

III. RESULTS AND DISCUSSIONS

The electronic properties such as the bandgap and the effective mass of the CNRs are very sensitive to the width of the ribbon. We chose semiconducting CNRs with various widths and performed a study of their bandstructures in order to investigate this issue. Fig. 3 shows the bandgap of the armchair CNRs vs. their width (left y-axis). Only for the

CNR width below a few nanometers, the bandgap reaches the values acceptable for the MOSFET operation. The effective mass of the first conduction subband increases as the width of CNR decreases as shown in the right *y*-axis of Fig. 3. Although decreasing the width of the CNRs will help to increase the bandgap and suppress band-to-band tunneling in a realistic CNR MOSFET, this will come at the expense of a reduction in the electron velocity, since this quantity is inversely proportional to the square root of the transport effective mass. In order to achieve reasonable bandgaps for MOSFET operation under designed V_{DS} of 0.4 V in this work, nanoribbons with widths of ~4 nm or less are required. Wider ribbons will give lower bandgap values, which will cause the device to suffer from band-to-band tunneling and degrade the I_{ON}/I_{OFF} ratio. In a subsequent study, we will examine the role of band-to-band tunneling and its impact on the OFF state, but in this paper, our focus is on the ON-state performance.

We compare the ballistic performance of CNR MOSFETs with W=2.2 nm (E_G=0.5 eV) and W=4.2 nm (E_G=*0.32* eV). In order to compare the ON-state performance of the two devices, and account for the difference in bandgaps, we fixed the OFF-current density to 0.06 µA/µm (according to the 90nm node of 2005 ITRS report [15]) by tuning the work function of the gate electrode for each device. Analytical estimates show that for all nanoribbons considered in this paper, the leakage current due to band-toband tunneling will be smaller then the above OFF-current density. Fig. 4(a) shows the simulated ballistic I_{DS} vs. V_G characteristics for these two devices. For comparison, we also include the simulated I_{DS}-V_G characteristics of an idealized, ballistic single-gate silicon MOSFET at the same operating bias of V_{DS}=0.4 V. We show both logarithmic scale (left axis) and linear scale (right axis) results in Fig. 4(a) to better illustrate the differences of the

devices. Due to the perfect gate electrostatics assumed, none of the devices suffer from DIBL, and the subthreshold swing is close to the ideal value of 60 mV/dec. Fig. 4(b) shows I_{DS} vs. V_{DS} for different gate biases for these devices. Both CNR MOSFETs with W=2.2 nm (square) and W=4.2 nm (circle) demonstrate very good MOSFET ON-state characteristics and high current values. Compared to an idealized, ballistic single-gate silicon MOSFET (triangle), these two types of CNR MOSFETs outperform silicon MOSFETs when operating at the same supply voltage (V_{DS}=0.4 V). For the same OFF-current density (I_{OFF}/W), the CNR MOSFETs deliver twice the ON-current densities (I_{ON}/W) (1300 and 1440 μA/μm for W=2.2 nm and W=4.2 nm, respectively) than a ballistic Si MOSFET (I_{ON}=680 μA/μm). This performance advantage over Si indicates that CNR MOSFETs will exhibit a smaller device delay. The lower operating bias for this type of devices will also allow for smaller power delay products (PDP).

The reason CNR MOSFETs can potentially outperform Si MOSFETs is because of the higher average velocity of the CNR compared to the average velocity of the ballistic silicon MOSFET. The current of ballistic devices can be evaluated ~~by~~ as the product of the average velocity times the number of carriers evaluated at the top of the barrier. Fig. 5 evaluates these two quantities. Fig. 5(a) shows the average velocity vs. gate voltage of the two CNR MOSFETs with W=2.2 nm (square) and 4.2 nm (circle), and of the Si MOSFET (triangle) at V_{DS}=0.4 V. The narrow (W=2.2 nm) and the wide (W=4.2 nm) CNR MOSFETs have 2 and 4 times, respectively, higher average velocities than the Si MOSFET. The differences in average velocities result from the different effective masses of the devices. The effective masses of the CNRs are $m^*=0.11m_0$ and $m^*=0.08m_0$ for W=2.2 nm and W=4.2 nm, respectively, where m_0 stands for the free electron mass. On

the other hand, the electron effective mass on the conduction band of silicon is $m^*=0.19m_0$. Fig. 5(b) shows the mobile charge per unit area in the channel versus V_G for these three devices. At the same gate bias, the Si MOSFET has higher mobile charge density than the CNR MOSFETs because of its larger quantum capacitance, which however is not high enough to compensate for the much higher velocities of the CNR MOSFETs. As a result, CNRs can provide higher ON-current densities in FET-like devices. Similarly, we study why the 4.2 nm width CNR MOSFET provides a slightly larger ON-current density than the 2.2 nm width one. Fig. 3(a) shows that the W=4.2 nm has lighter effective mass, and therefore higher injection velocity as shown in Fig. 5(a). Although the mobile charge density in the 2.2 nm width CNR MOSFET is higher than that of the 4.2 nm one, it is not enough to compensate its reduced injection velocity compared to the wider ribbon.

IV. CONCLUSION

In this study, we investigated the upper limit performance of CNR MOSFETs using a nearest-neighbor TB method for bandstructure calculation and a ballistic “top-of-the-barrier” model. We found that the bandstructure and consequently the electronic properties of carbon nanoribbons are a strong function of their transport orientation and their width quantization. Although several fabrication challenges must be addressed in synthesizing single carbon layer devices with well controlled widths and building these specific size CNRs in parallel to reach desired operation current, these types of devices could be an alternative to the carbon nanotube technology which currently faces serious chirality control challenges. Semiconducting CNR MOSFETs have potential applications

as digital switches if widths of a few nanometers can be achieved in order to provide a large sufficient bandgap. Wider CNRs gives very small bandgaps and may be suitable for high power applications only, their narrow bandgap will enhance band-to-band tunneling and increased subthreshold leakage current. Our ballistic MOSFET calculations show that based on bandstructure alone, CNRs should be able to outperform silicon MOSFETs in terms of drive current capabilities by over 100%.

ACKNOWLEDGEMENTS

This work was supported by the MARCO Focus Center on Materials, Structures, and Devices. The authors would like to thank Siyuranga Koswatta, and Kurtis Cantley for helpful discussions.

Reference

[1] P. L. McEuen, M. S. Fuhrer, and H. Park, “Single-walled carbon nanotube electronics,” IEEE Trans. *Nanotechnology,* vol. **1**, pp. 78-85, March 2002.

[2] J. A. Misewich, R. Martel, Ph. Avouris, J. C. Tsang, S. Heinze, and J.Tersoff, “Electrically induced optical emission from a carbon nanotube FET,” *Science,* vol. **300**, pp. 783-786, May 2003. J. Chen, V. Perebeinos, M. Freitag, J. Tsang, Q. Fu, J. Liu, and P. Avouris, “Bright infrared emission from electrically induced excitons in carbon nanotubes,” *Science,* vol. **310**, pp. 1171-1174, Nov. 2005.

[3] A. Javey, J. Guo, Q. Wang, M. Lundstrom, and H. Dai, “Ballistic carbon nanotube field-effect transistors,” *Nature,* vol. **424**, pp. 654-657, Aug 2003.

[4] J. Li, Q. Ye, A. Cassel, H.T. Ng, R. Stevens, J. Han, ans M. Meyyappan, “Bottom-up approach for carbon nanotube interconnects,” *Appl. Phys. Lett*., vol. **82**, pp. 2491-2493, Apr. 2003.

[5] J. E. Jang, S. N. Cha, Y. Choi, G. A. J. Amatatunga, D. J. Kang, D. G. Hasko, J. E. Jung, and J. M. Kim, “Nanoelectromechanical switches with vertically aligned carbon nanotubes,” *Appl. Phys. Lett.,* vol. 87, 163114, Oct. 2005.

[6] J. Kong, N. Franklin, C. Chou, S. Pan, K. Cho and H. Dai, “Nanotube molecular wires as chemical sensors,” *Science,* vol. **287**, pp. 622-625, Jan 2000.

[7] R. Saito, G. Dresselhaus, M. Dresselhaus, *Physical Properties of Carbon Nanotubes*, Imperial College Press, London (1998).

[8] M. Fujita, K. Wakabayashi, K. Nakada, and K. Kusakabe, “Peculiar localized state at zigzag graphite edge,” *Journal of the Physical Society of Japan,* vol. **65**, pp. 1920-1923, July 1996.

[9] B. Obradovic, R. Kotlyar, F. Heinz, P. Matagne, T. Rakshit, D. Nikonov, M. D. Giles, and M. A. Stettler, “Analysis of graphene nanoribbons as a channel material for field-effect transistors,” *Appl. Phys. Lett.,* vol. **88**, 142102, Apr. 2006.

[10] K. Wakabayashi, “Electronic transport properties of nanographite ribbon junctions,” *Phys. Rev. B,* vol. **64**, 125428, Sep. 2001. K. Nakada, M. Fujita, G. Dresselhaus, M. Dresselhaus, “Edge state in graphene ribbons: Nanometer size effect and edge shape dependence,” *Phys. Rev. B.* vol. **54**, 17954, Jun. 1996.

[11] C. Berger, Z. Song, X. Li1, X. Wu, N. Brown, C. Naud, D. Mayou, T. Li, J. Hass, A. N. Marchenkov, E. H. Conrad, P. N. First and W.A. de Heer, “Electronic confinement and coherence in patterned epitaxial graphene,” *Sienc,* vol. **312**, pp. 1191-1196, May 2006; Y. Zhang, J. P. Small, W. V. Ponyius, and P. Kim, “Fabrication and electric-field-dependent transport measurements of mesoscopic graphite,” *Appl. Phys. Lett*,. vol. **86,** 073104, Feb. 2005.

[12] A. Rahman, J. Guo, S Datta, and M. Lundstrom, “Theory of ballistic nanotransistors,”*IEEE Trans. Electron Devices,* vol. **50**, pp. 1853-1164, Sep. 2003.

[13] K. Kobayashi, “Electronic structure of a stepped graphite surface,” *Phys. Rev. B,* vol. **48**, pp.1757-1760, Mar.1993.

[14] K. Wakabayshi and M. Sigrist, "Zero-Conductance Resonances due to Flux States in Nanographite Ribbon Junctions,"*Phys. Rev. Lett.,* vol. **84,** pp. 3390-3393, July 2000.

[15] Semiconductor Industry Association, "International Roadmap for Semiconductors," 2005. Available: http://public.itrs.net/

FIGURE CAPTIONS

Fig. 1: (a) and (d) the atomic structure of armchair and zigzag carbon nanoribbon, respectively. The nanoribbon is characterized by its transport direction and specified by n, the number of atoms in transverse direction. The unit cell is shown by the dashed rectangle for each case. Hydrogen atoms are assumed to bond with all carbon atoms at the edge in order to eliminate surface states contributed by σ states. (b) The electronic structure of armchair CNR with 1nm width (N=9), which shows semiconducting behavior. (c) The electronic structure of armchair CNR with 0.9nm width (N=8), which shows semi-metallic behavior. (e) The electronic structure of zigzag CNR with 1nm width (N=10), which shows semi-metallic property. (f) The electronic structure of zigzag CNR with 0.9nm width (N=9), which shows localized states in the bandgap.

Fig. 2: (a) The top-of-barrier ballistic MOSFET model. The charge on the top of the barrier and the ballistic current is calculated by the positive and negative going fluxes injected from the source and the drain respectively. (b) A schematic diagram of the simulated carbon nanoribbon MOSFETs. The source and drain are assumed to be heavily doped nanoribbon contacts while the channel is intrinsic. The oxide thickness is 1.1nm. (c) Top view of (b).

Fig. 3: Bandgap and effective mass dependence on the width of CNRs. Due to quantum confinement effects, the bandgap (left vertical axis) and effective mass of the 1st subband (right vertical axis) of armchair CNR increase as the width of armchair CNR decreases.

Here m_0 stands for the free electron mass. Values of width are discrete, the curves used only to guide the eye.

Fig. 4: (a) The ballistic current-density vs. gate bias (V_G) of 2.2nm width (square), 4.2nm width (circle) CNR MOSFETs, and Silicon MOSFET (triangle) devices. Both log scale (left axis) and linear scale (right axis) are presented. The simulations are performed at the same OFF-current (I_{OFF}=0.06μA/μm) for all cases. (b) The I_D-V_{DS} characteristics of the three types of MOSFETs for V_G varied from 0V to 0.4V in steps of 0.2V.

Fig. 5: (a) The average carrier velocity vs. V_G at V_{DS}=0.4 V for the planar CNR MOSFETs with W=2.2nm (square) and 4.2nm (circle), and a Si planar MOSFET (triangle). (b) The mobile charge in the channel of MOSFETs vs. V_G at V_{DS}=0.4 V for the three types of devices.

Fig. 1. Liang, Neophytou, Nikonov, and Lundstrom

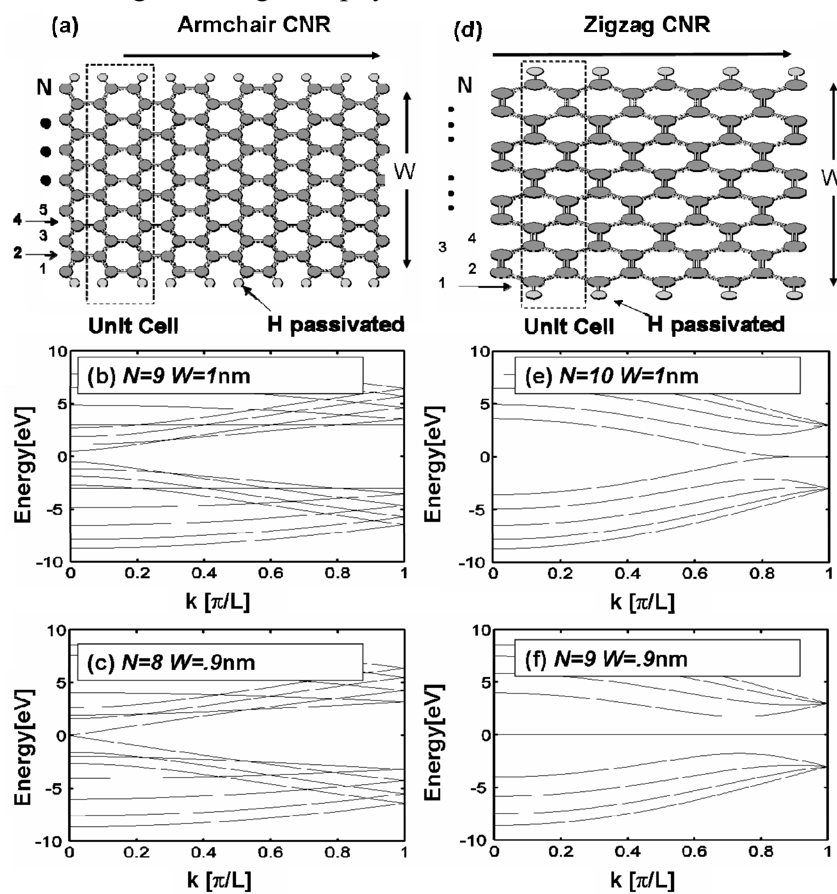

Fig. 2. Liang, Neophytou, Nikonov, and Lundstrom

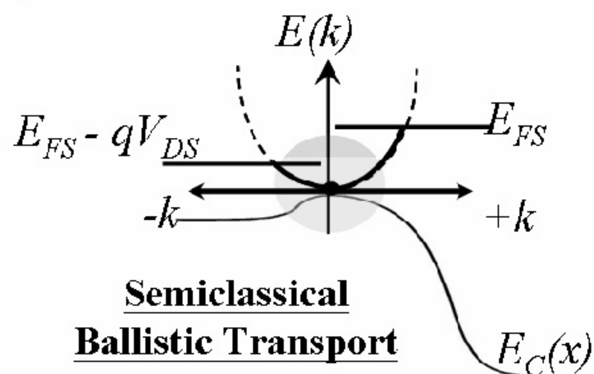

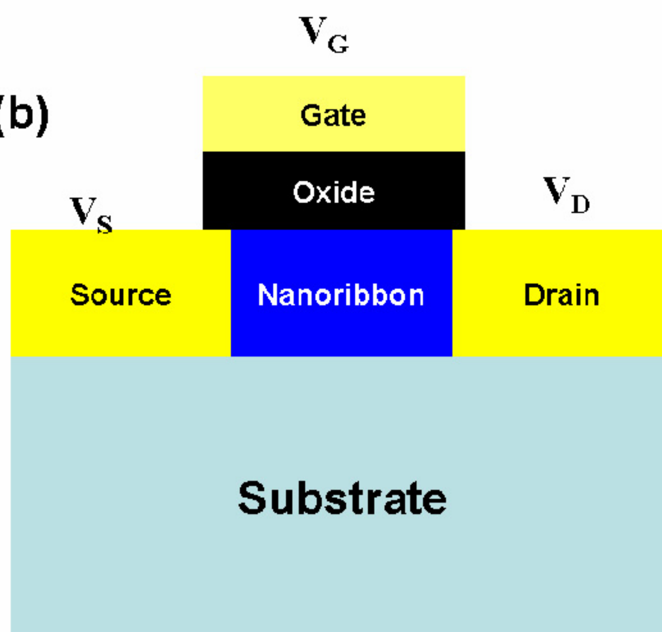

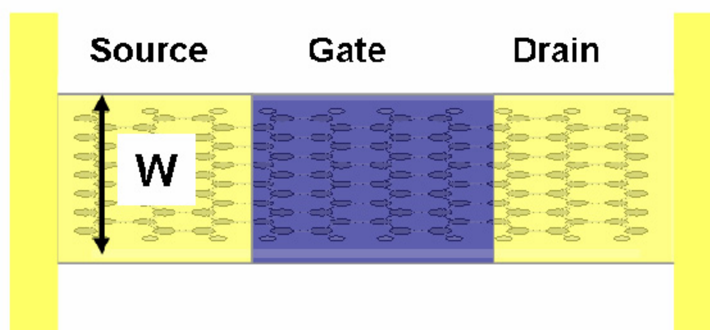

Fig. 3. Liang, Neophytou, Nikonov, and Lundstrom

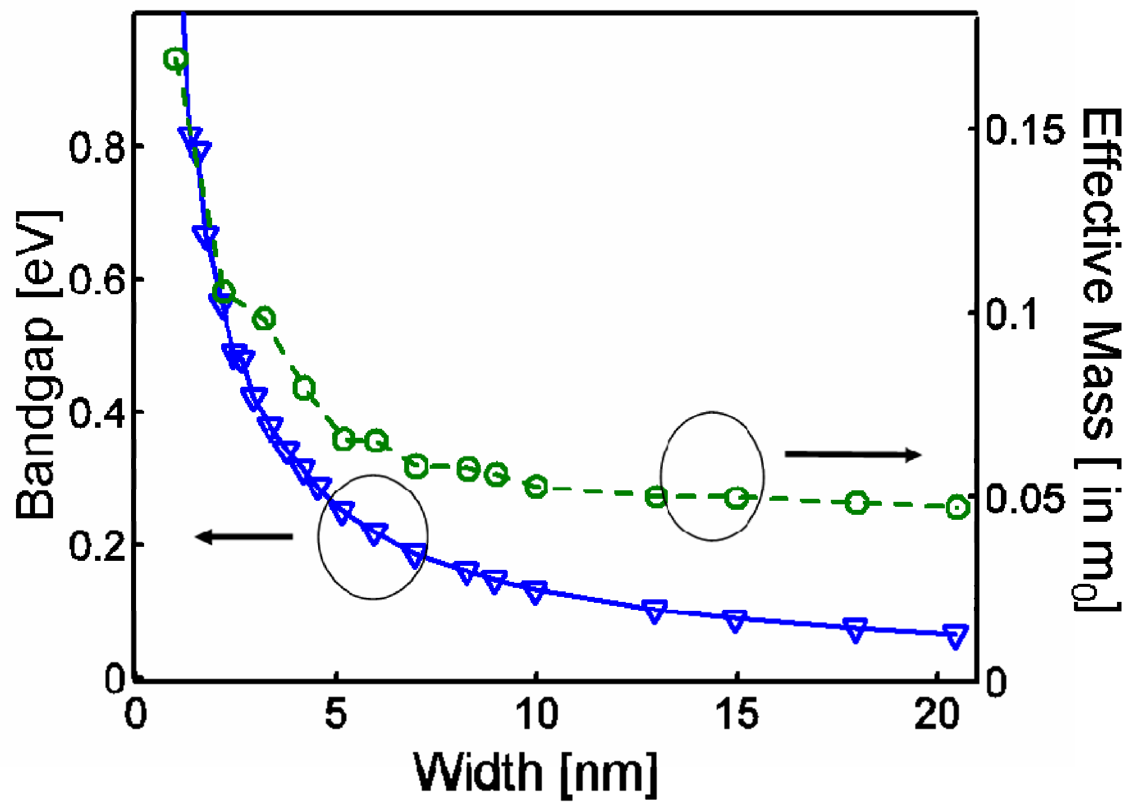

Fig. 4. Liang, Neophytou, Nikonov, and Lundstrom

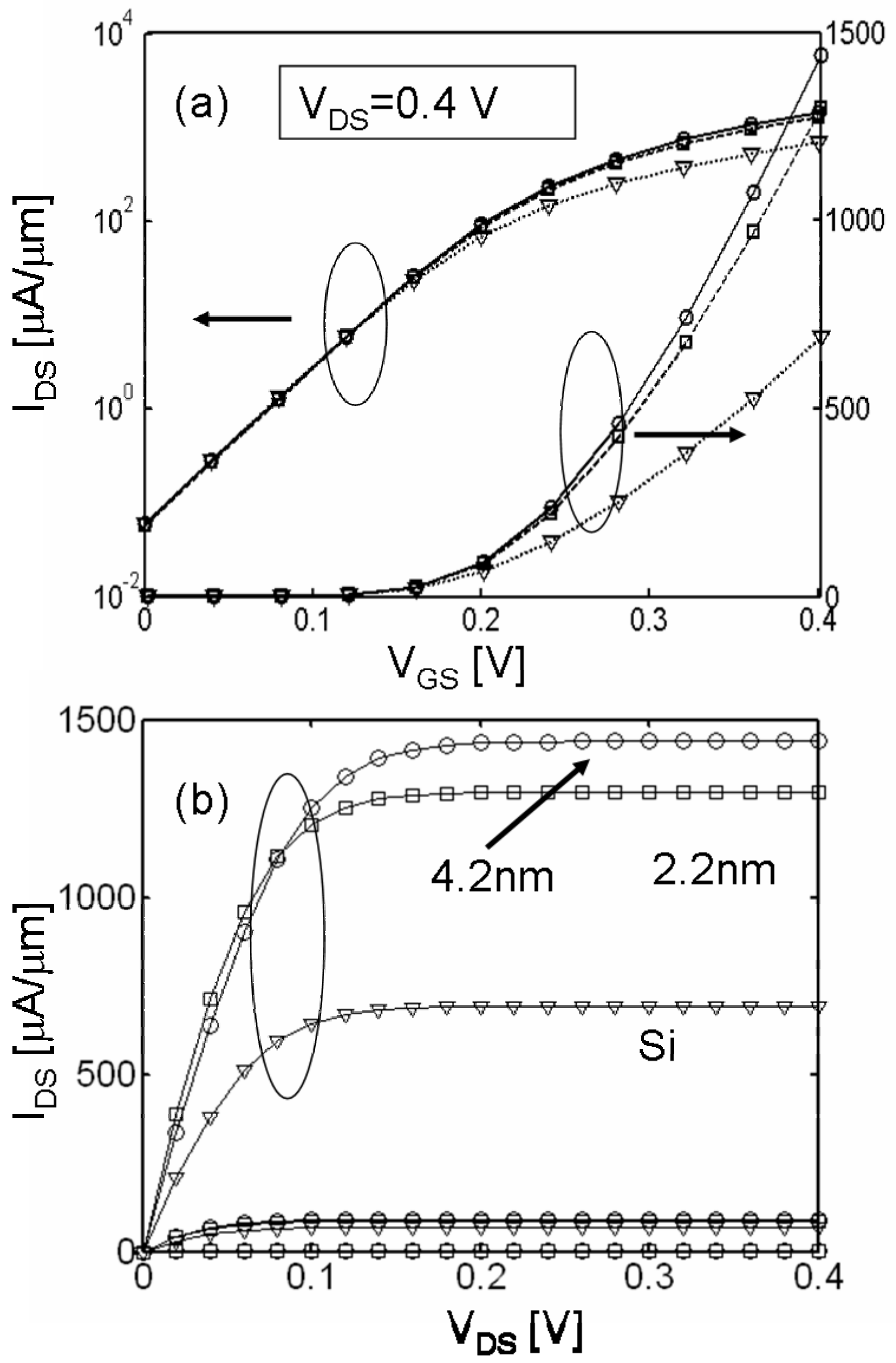

Fig. 5. Liang, Neophytou, Nikonov, and Lundstrom